Available online at www.sciencedirect.com

ScienceDirect

Advances in Space Research 72 (2023) 5490–5502

ADVANCES IN SPACE RESEARCH (a COSPAR publication)

www.elsevier.com/locate/asr

Multi-scale response of the high-latitude topside ionosphere to geospace forcing

Jaroslav Urbar [a,f], Luca Spogli [a,e,1,*], Antonio Cicone [a,b,g], Lasse B.N. Clausen [c], Yaqi Jin [c], Alan G. Wood [d], Lucilla Alfonsi [a], Claudio Cesaroni [a], Daria Kotova [c], Per Høeg [c], Wojciech J. Miloch [c]

[a] Istituto Nazionale di Geofisica e Vulcanologia, Via di Vigna Murata 605, 00143 Rome, Italy
[b] DISIM, University of L'Aquila, via Vetoio 1, 67100 L'Aquila, Italy
[c] University of Oslo, Problemveien 7, 0315 Oslo, Norway
[d] Space Environment and Radio Engineering Group (SERENE), University of Birmingham, B15 2TT Birmingham, UK
[e] SpacEarth Technology, Via di Vigna Murata, 00143 Rome, Italy
[f] Institute of Atmospheric Physics of the Czech Academy of Sciences, Boční II 1401, 14100 Prague, Czech Republic
[g] Istituto di Astrofisica e Planetologia Spaziali, INAF, Via del Fosso del Cavaliere 100, 00133 Rome, Italy

Received 31 March 2022; received in revised form 14 June 2022; accepted 18 June 2022
Available online 26 June 2022

Abstract

We investigate the response of the topside ionosphere, auroral and polar sectors, to the forcing of the geospace during September 2017. Specifically, we aim at characterizing such a response in terms of the involved spatial scales and of their intensification during the different auroral and polar cap activity conditions experienced in the selected month, that is characterized by severe geomagnetic storm conditions. For our purposes, we leverage on and compare various in situ plasma density data products provided by the Swarm constellation of the European Space Agency (ESA). The spatio-temporal variability of the involved scales in the plasma density observation is featured through the application of the Fast Iterative Filtering (FIF) signal decomposition technique and, for the first time in the ionospheric field, of a FIF-derived dynamical spectrum called "IMFogram". The instantaneous time-frequency representation provided through the IMFogram illustrates the time development of the multi-scale processes with spatial and temporal resolutions higher than those obtained with traditional signal processing techniques. To demonstrate this, the IMFogram is tested against Fast Fourier and Continuous Wavelet Transforms. With our fine characterization, we highlight how scale cascading and intensification processes in the plasma density observations follow the ionospheric currents activity, as depicted through the auroral activity and polar cap indices, and through the field-aligned currents data product provided by Swarm.

Keywords: Plasma density; Topside ionosphere; Swarm satellite; Time-frequency analysis

1. Introduction

The ionosphere is a dynamical system exhibiting nonlinear couplings with the other "spheres" characterizing the geospace environment. Such nonlinearity manifests also through the non-trivial, largely varying range of spatial and temporal scales (Moen et al., 2012). Those variations are modulated by the drivers of the phenomena character-

* Corresponding author.
E-mail addresses: urbar@ufa.cas.cz (J. Urbar), luca.spogli@ingv.it (L. Spogli), antonio.cicone@univaq.it (A. Cicone), lasse.clausen@fys.uio.no (L.B.N. Clausen), yaqi.jin@fys.uio.no (Y. Jin), a.wood.1@bham.ac.uk (A.G. Wood), lucilla.alfonsi@ingv.it (L. Alfonsi), claudio.cesaroni@ingv.it (C. Cesaroni), daria.kotova@fys.uio.no (D. Kotova), per.hoeg@fys.uio.no (P. Høeg), w.j.miloch@fys.uio.no (W.J. Miloch).
[1] SpacEarth Technology, www.spacearth.net.

https://doi.org/10.1016/j.asr.2022.06.045
0273-1177/

izing the Solar Wind-Magnetosphere-Ionosphere-Thermosphere (SW-M-I-T) coupled system. In this work, we aim at characterizing the multi-scale nature of the processes involved in the dynamical response to the geospace forcing of the high-latitude topside ionosphere. This characterization arises in the frame of the Swarm-VIP (Variability of Ionospheric Plasma) project, that has been funded by the European Space Agency (ESA), contract 4000130562/20/I-DT "Swarm+4D Ionosphere", to exploit the data of the Swarm constellation (Friis-Christensen et al., 2008) for advancing the understanding and the characterisation of ionosphere processes, and the consequent modelling and forecasting capability in the SW-M-I-T coupling context. Thus, we characterize the scales involved in the topside ionosphere processes at the Swarm A altitudes (about 470 km) in the polar and auroral sector of both hemispheres. Specifically, we aim at identifying if there are some frequencies embedded in Swarm plasma density data that are enhanced under increased geospace forcing. Those frequencies translate into spatial scales along the Swarm flight direction and possible drivers of such intensifications can be identified. This characterization has been inspired by previous works that addressed the scale-wise response of the ionosphere to the geospace forcing. Among them, Piersanti and co-authors (Piersanti et al., 2017) identified that the ionospheric Total Electron Content (TEC) measured by a network of receivers for Global Navigation Satellite System (GNSS) signals covering mainly the European sector does not react to solar transients as a whole. In fact, they identified a peculiar mode in TEC data having a period of about 45 min which intensifies right after the Sudden Impulse of the 2015 Saint Patrick's Day storm. Spogli and co-authors (Spogli et al., 2019) studied the multi-scale variability of the low-latitude ionosphere with GNSS scintillation data and they speculated on the possible relationship between forcing factors from the geospace and the ionospheric response. They identified resonant modes in the Akasofu's parameter as the geospatial driver modulating the scale-wise response of amplitude scintillation data recorded by a receiver located below the southern crest of the equatorial ionospheric anomaly in the South American sector. Those two works are characterized by using the integrated ionospheric information (TEC and scintillation) embedded in a trans-ionospheric signal emitted at an altitude of about 20000 km by the slowly varying geometry of observation (with respect to the fast orbiting Swarm), that, at a very first approximation, allows investigating a single ionospheric sector per each GNSS satellite-receiver couple.

Being inspired by those works and bearing in mind the considerations above, to identify frequencies and scales embedded in the Swarm electron density (*Ne*) data, we leverage on the use of the Fast Iterative Filtering (FIF) technique ((Cicone, 2020; Cicone and Zhou, 2021)). Beyond the already cited works, FIF, together with its predecessor ALIF (Adaptive Local Iterative Filtering, (Cicone et al., 2016)) or its multivariate version (MvFIF, (Cicone and Pellegrino, 2022)), has been successfully used in the ionospheric domain to conduct time-frequency, spectral and multi-scale analyses (see, e.g., (Ghobadi et al., 2020b; Piersanti et al., 2018; Spogli et al., 2019; Ghobadi et al., 2020a; Materassi et al., 2019; Urbar et al., 2021)).

The FIF technique provides an efficient decomposition of nonlinear non-stationary signal into functions oscillating around zero called in Mathematics Intrinsic Mode Functions, but we will rather call them here Components (IMCs) to remove ambiguity, as we also discuss later, with the interplanetary magnetic field (IMF). From the FIF decomposition, the so called IMFogram can be derived (Cicone et al., 2022). The IMFogram is an analogue of the spectrogram that can be computed on the IMC decomposition to identify the local frequency and amplitude information of a signal simultaneously. In other words, the IMFogram provides frequency (and, then, scale) identification with accurate resolution in both time and frequency domains. Basic principles and further details about FIF and IMFogram are recalled in Section 3.1.

To illustrate how the FIF/IMFogram-based scale characterization allows obtaining the finest time-scale resolution, we also provide in Section 3.2 a comparison with dynamical spectrum of plasma density data obtained with standard techniques like the Fast Fourier Transform (FFT) and the Continuous Wavelet Transform (CWT).

The period selected for the analysis is the whole September 2017, that is characterized by significant disturbances of the geospace environment. Besides influenced by the solar flares being among the strongest of Solar Cycle 24 (Berdermann et al., 2018), during 7–8 September, two Interplanetary Coronal Mass Ejections (ICMEs) struck the Earth's magnetosphere (Wu et al., 2019), triggering severe geomagnetic storm conditions and significant variations in the ionospheric environment at all latitudinal sectors (Tassev et al., 2018; Aa et al., 2018; Linty et al., 2018; Jimoh et al., 2019; Li et al., 2018; Alfonsi et al., 2021; Mosna et al., 2020). Later in the month, the fast solar wind-initiated corotating interaction region (CIR) disturbed the geospace on 27 and 28 September 2017, generating moderate geomagnetic storm conditions (Shinbori et al., 2020).

2. Data

ESA's Swarm constellation is constituted by three satellites (Swarm A, Swarm B and Swarm C) flying at different heights in near-polar orbits (inclination ~87°). The Swarm A and C pair fly side-by-side, separated by 1.4° in longitude (i.e., ~150 km at the equator), at an altitude of about 470 km in the topside ionosphere. The Swarm B satellite flies at about 510 km and its longitudinal distance with Swarm A-C drifts during the mission lifetime. Despite being conceived mainly to investigate Earth's geomagnetic field and its temporal evolution; the constellation orbital characteristics are well suited to study the auroral and polar ionosphere. We concentrate on this ionospheric sec-

tor, identified by magnetic latitudes (*MLat*) above 55°, because it is directly exposed to variations triggered by the SW-M-I coupling. To investigate this sector, we leverage on the *in-situ* plasma density measurements provided by the instruments onboard the satellites. The Swarm Electric Field Instrument (EFI) provides, among other measurements, the in-situ plasma density by two Langmuir Probes (LP) and by Thermal Ion Imagers (TII) (Knudsen et al., 2017), being TII faceplates used as a plasma density detector (FP) (Buchert and Nilsson, 2017). Overall availability of the 2 Hz LP plasma density data is almost continuous and very few data gaps are present, whereas the 16 Hz plasma density provided by the FP detector is only available when the TIIs were not operating. Generally LP shows a good agreement with the FP, except having an offset during the measurements on the night-side (see Fig. 8 in (Catapano et al., 2022)). There are some specific differences between the LP plasma density data products being used, interested readers are referred to the Annex A with the reasoning of data selection adopted in the paper (see Fig. 8).

The Swarm satellite constellation, allows determining intensity and sign of the radial currents vector magnetic field measurements from the onboard magnetometers. Thus, Swarm considered measurements includes also local field-aligned current (FAC) estimation at a 1 Hz rate (Ritter et al., 2013; Kervalishvili and Park, 2017), that is useful to separate the polar and the auroral sector while interpreting the results. We leverage also on the use of the Ionospheric Plasma IRregularities (IPIR) data product (Jin et al., 2022) that contains information about the plasma density gradients at different spatial scales along the Swarm orbit. We use these gradients for the purposes of comparing it with the scale reconstructed through IMFogram as detailed later in the Section 3.1.

As already noted, the measurements of Swarm A are used throughout this paper. We have evaluated that the closely separated Swarm C provides very similar results whereas the Swarm B (orbiting at higher altitudes and covering a different longitudinal sector) shows similar features in terms of involved spatial scales.

As already mentioned in the Introduction section, we consider the Swarm high-latitude tracks of both hemispheres during September 2017. To characterize the geospace environment and the ground magnetic variations induced by its modifications, the following quantities have been considered: (i) the SymH index, (ii) the z-component of the Interplanetary Magnetic Field (Bz) measured by the Magnetic Field Experiment (MAG) (Smith et al., 1998) onboard the Advanced Composition Explorer (ACE) and time-shifted to the nose of the Earth's Bow Shock; (iii) the Geomagnetic Auroral Electrojet (AE); and (iv) the polar cap (PC) index for both hemispheres (PCN and PCS). Reviews concerning the geomagnetic indices cited above can be found in (Perrone and Franceschi, 1998 and Kauristie et al., 2017). Details about the PC index unified calculation procedure for both hemispheres is given in (Troshichev et al., 2006).

3. Methods

3.1. Fast Iterative Filtering (FIF) and IMFogram

As we mentioned in the introduction, IMFogram (Cicone et al., 2022) allows to obtain crisper and more focused time-frequency representation of non-stationary signals with respect to classical techniques like Fast Fourier Transform (FFT) spectrograms and the Continuous Wavelet Transform (CWT). The IMFogram's better performance is based on a "divide et impera" approach, which is completely data driven. A given nonlinear non-stationary signal is first decomposed into simple oscillating functions called Intrinsic Mode Components (IMCs) by means of the iterative application of proper filters (Cicone and Zhou, 2021), which guarantee the preservation of the L1 Fourier energy of the signal (Cicone et al., 2022). Then, each IMC is analyzed from a time-frequency point of view producing the so called IMFogram representation.

In particular, the IMFogram matrix A is computed based on the following formula

$$A\left(LF_{I_j}^{(k)}, j\right) = \widetilde{A}\left(LF_{I_j}^{(k)}, j\right) + LA_{I_j}^{(k)}, \quad \forall j = 1, 2, \ldots, N$$

where $\widetilde{A}$ is the previously computed IMFogram matrix, which is initially set to have all zero entries, I_j is a sliding time window, N is the number of IMCs, $LA_{I_j}^{(k)}$ is the local amplitude on I_j of the k-th IMC, computed as the weighted average of the envelope interpolating the local maxima of $|\mathrm{IMC}_k|$ on the time interval I_j, where, as weights, we use the amplitudes of IMC_k itself on the time interval I_j. Furthermore, $LF_{I_j}^{(k)}$ represents the local frequency on I_j of the k-th IMC as the weighted average on the time interval I_j of the envelope interpolating the set of points $\left\{\left(\mathrm{zx}_i^{(k)}, \frac{1}{2\triangle \mathrm{zx}_i^{(k)}}\right)\right\}_i$, where $\triangle \mathrm{zx}^{(k)}$ represents the relative distances between subsequent zero crossings $\left\{\mathrm{zx}_i^{(k)}\right\}_i$ in the IMC.

Even though the frequency in the IMFogram is computed as a first order approximation, since it is based on a weighted average of the interpolated relative distances between subsequent zero crossings, it proves to provide a more accurate time and frequency localization than FFT spectrogram and CWT methods. This is due to the intrinsic linearity of these last two techniques (Cicone et al., 2022). Furthermore, the IMFogram representation of a signal has been recently proved convergent to the FFT spectrogram as the stopping criterion in the FIF decomposition tends to zero (Cicone et al., 2022), showing that the IMFogram is a special generalization of the FFT spectrogram.

We point out that the FIF method, since it is based on FFT, assumes periodicity at the boundaries of the signal under study. To overcome this limitation, Stallone et al. (2020) proposed an extension approach that reduce drastically the boundary errors. Alternatively, if the data nearby

the boundaries are not required, then data windowing can be applied similarly as e.g. for the spectrogram.

3.2. IMFogram comparisons with CWT and FFT spectrograms

To show the finer time-frequency (scale) representation of the IMFogram than the traditional FFT spectrograms and CWT, Fig. 1 provides an example of comparison between the various techniques (FIF, CWT, FFT) on a *Ne* data chop covering the investigated high latitude sectors ($|MLat| > 55°$). *Ne* data refer to 2 Hz Langmuir probe (indicated with a LP superscript in the figure) plasma density measurements in the red curve of the top panel, while the green line shows the 16 Hz plasma density provided by the faceplate detector (FP superscript). The orange dashed line indicates the *MLat* and illustrates how this Swarm track (the track number in title refers to subsequent high-

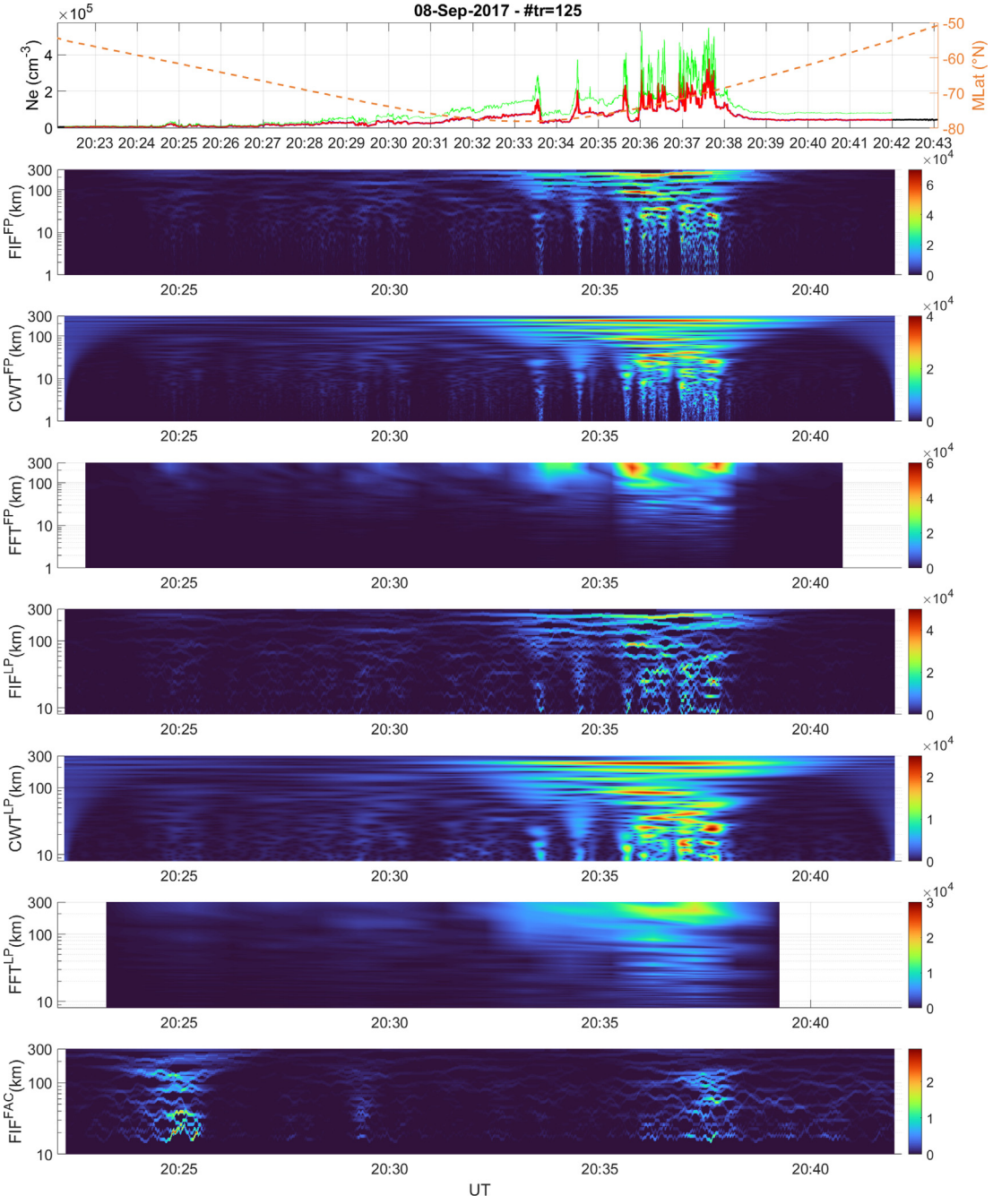

Fig. 1. Comparison of IMFogram outputs using FIF with traditional CWT and FFT spectrograms, colour bars showing the intensities of scales in A.U. Top panel shows satellite magnetic latitude by orange line, the 2 Hz Langmuir probe (LP) plasma density measurements in red, while the green line shows the 16 Hz plasma density provided by the faceplate detector (FP). The following 3 middle panels demonstrate the intensities of scales constructed by FIF, CWT and FFT, respectively, for the 16 Hz FP. The following 3 middle panels similarly demonstrate those intensities, but for the LP. The IMFogram at the bottom shows the intensities of the FAC.

latitude observations within interval of focus, 5–11 September) refers to the southern hemisphere, as crossed between 20:22 UT and 20:43 UT on 8 September 2017 during the storm recovery phase (as bottom panels with SymH of Figs. 3–5 show). To illustrate the relative contributions of the polar cap and auroral sectors, in the bottom panel we report the IMFogram of the FAC product. We converted the frequencies to spatial scales along the Swarm A orbit by knowing its speed of 7.5 km/s.

Fig. 1 demonstrates that FIF provides an enhanced level of details that can be neither captured by the FFT spectrogram nor by the CWT. Comparing the IMFogram with the spectrograms it is evident that the latter methods provide the intensifications which are considerably more spread in both scale and time. This and other limits of FFT and CWT versus IMFogram are detailed in (Cicone et al., 2022). Here we simply note that, in this figure, the signal pre-extensions were not performed for the CWT (although possible), they were applied only for the FIF. Therefore, the signal decoherence at the CWT boundaries should be disregarded. FFT spectrogram plots report a shorter time interval as the technique needed the surrounding parts of data, unavailable at the boundaries (pre-extension could resolve the FFT issue as well).

3.3. Selection of scales and related geophysical parameters

Fig. 1 highlights a cascading process from scales > 10 km down to smaller scales during strong events, although FP also at times shows intensifications of the shorter wavelengths, i.e. representing lower spatio-temporal scales than LP can resolve (1–7 km). FFT is not even able to depict this cascading to smaller structures induced by the presence of the steep *Ne* gradients, which FIF and CWT show well. Here we remind that, despite the FP acts like a planar LP and can record ionospheric irregularities of scales sizes below to 0.5 km (along the track), it can operate only when the TII is inactive (Knudsen et al., 2017). This results in the fact that FP data are available only about half of the time, that was another reason to use the LP for providing as much complete storm development timeline as possible. In the following figures, we use then *Ne* samples measured at a 2 Hz rate by the Swarm A satellite, only covering the sector $|MLat| > 55°$, therefore including mainly auroral and polar cap ionospheric sectors of both hemispheres. The plots include some data from the mid-latitude region but, as the level of intensification in that region was relatively smaller, this did not significantly affect the results. The intervals in polar cap or auroral region are well separable using the FAC characteristics, shown also by the FAC IMFogram at the bottom of all case studies (Figs. 1,3,4,5).

The IPIR products include the *Ne* gradients along the Swarm tracks evaluated to correspond with different spatial intervals, namely 20 km, 50 and 100 km (*gradNe@XXkm*). We also investigate the possibility to use the information provided by the IMFogram as a proxy to identify the behaviour of the *Ne* gradient at each scale identified by FIF decomposition. To that scope, in Fig. 2 we provide an example of comparison between the absolute value of the *gradNe*@20 km (bottom plot), *gradNe*@50 km (middle plot) and *gradNe*@100 km (top plot) with a time profile of the IMFogram information sliced at the 3 spatial scales, i.e. $FIF^{Ne@XXkm}$. The values of $FIF^{Ne@XXkm}$ follow the $|gradNe@XXkm|$ in a reasonable way, providing further information on the potential usability of FIF-based parameters as proxy for each scale-wise ionospheric parameter.

4. Ionospheric scales intensification variations during September 2017

We remind that we aim at characterizing how the spatial scales identified through the time-scale analysis provided

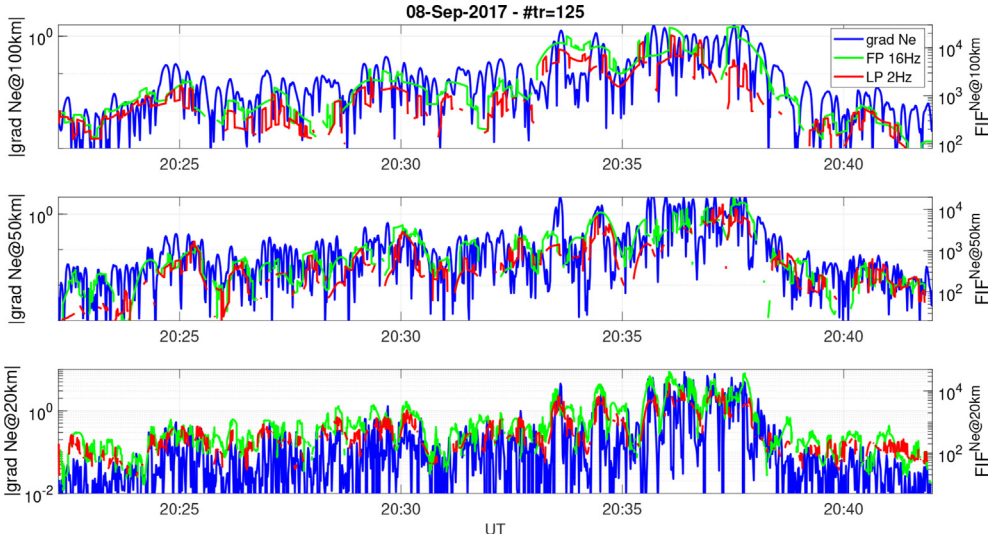

Fig. 2. *GradNe@XXkm* (blue line) compared with respective IMFogram scales $FIF^{Ne@XXkm}$ (in green using the FP and in red the LP data) representing spatial scales at 100, 50 and 20 km in the top, middle and bottom panels, respectively. Shown is the same time range as in Fig. 1.

by FIF/IMFogram technique intensify as a response of the geospace forcing. September 2017 was selected for this study due to significant ionospheric effects, exceptional compared to other events in the solar cycle 24.

First we show the single-track snapshots of ionospheric scales intensifications at high-latitudes during the storm in Figs. 3,4,5 and 1. Subsequently, these snapshots are track-length normalised track-integrated per each frequency represented by spatial scale, and the resulting statistics during the selected period shown in Fig. 6 and 7.

Fig. 3 shows single-track snapshot along with the conditions before the storm onset. At the first panel is shown *Ne* data chop covering the investigated high latitude sectors ($|MLat| > 55°$). *Ne* data refer to 2 Hz Langmuir probe (indicated with a LP superscript in the figure) plasma density measurements by the red curve. The orange dashed line indicates the *MLat* and illustrates how this Swarm track refers to the southern hemisphere, as crossed between 21:40 UT and 22:00 UT on 6 September 2017. The second panel shows IMFogram where one can identify the specific scales (e.g., at 100 km scale) including higher levels of background activity already during these quiescent conditions. The following 2 panels provide comparison with CWT and FFT spectrogram generally supporting the main features provided by IMFogram at the second panel. To illustrate the relative contributions of the polar cap and auroral sectors, the following panel reports the IMFogram of the FAC product where the main FAC activity is related to the intensifications in the *Ne* scales shown above it. Last two bottom panels (same for Figs. 3–5) report the condi-

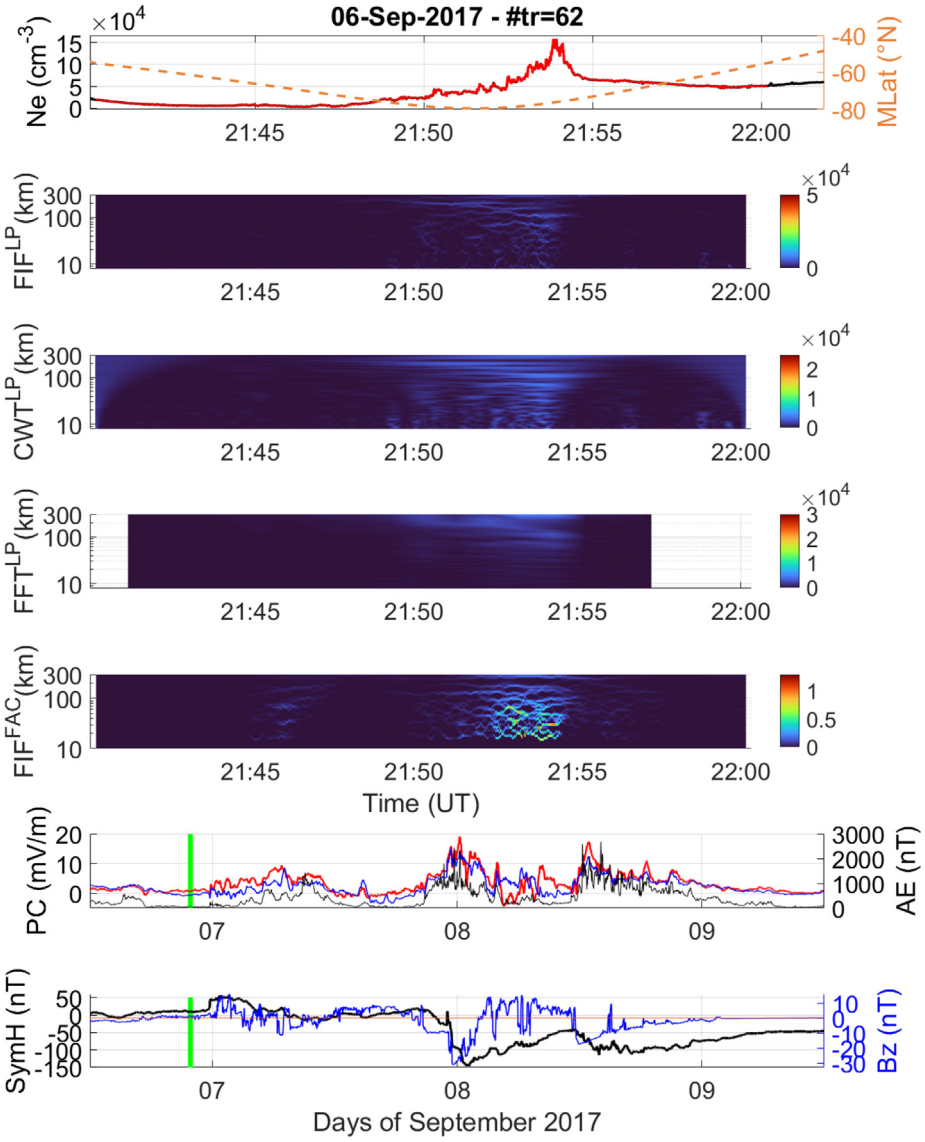

Fig. 3. Pre-storm conditions without significant ionospheric plasma scale intensifications: Top panel shows the 2 Hz LP electron density measurements, following 3 middle panels demonstrate the intensities of scales constructed by FIF, CWT and FFT, respectively. Following IMFogram shows the intensities of the FAC. Last two panels show the high-latitude geomagnetic activity (The AE, the PC North and PC South indices are printed in black, blue, and red, resp.), SymH and the IMF Bz conditions, where the green lines indicate the time of the Swarm track.

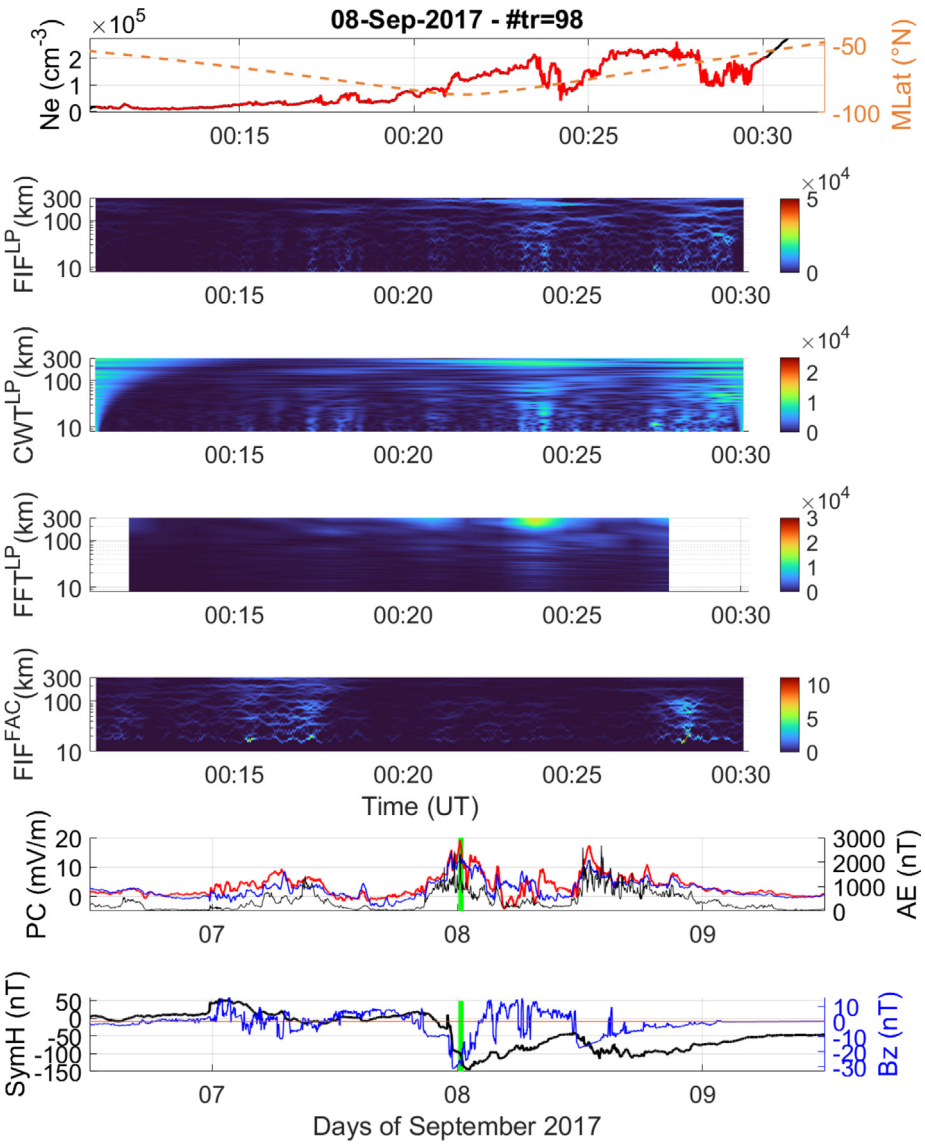

Fig. 4. Storm main phase and ionospheric plasma scale intensifications: Top panel shows the 2 Hz LP electron density measurements, following 3 middle panels demonstrate the intensities of scales constructed by FIF, CWT and FFT, respectively. Following IMFogram shows the intensities of the FAC. Last two panels show the high-latitude geomagnetic activity (The AE, the PC North and PC South indices are printed in black, blue, and red, resp.), SymH and the IMF Bz conditions, where the green lines indicate the time of the Swarm track.

tions of IMF and geomagnetic activity from September 6 to 10, where the green lines indicate the time of the Swarm track shown in panels above. The bottom panel provides the general storm conditions showing IMF Bz and SymH index, the panel above it shows specifically the high-latitude magnetic activity indices (providing the north-hemisphere related AE, the PC North and PC South in black, blue, and red, respectively).

The arrival of ICME shock produced a Sudden Storm Commencement (SSC) (Mosna et al., 2020) on the geomagnetic field on 6 September around 23:50 UT As shown in Fig. 3 bottom panel, the IMF Bz was positive not allowing significant dayside SW-magnetosphere reconnection, so initially only low geomagnetic activity was observed as seen on the SymH index. Later the storm triggered intensification of ionospheric currents and polar cap activity, as notable from the behaviour of AE and PC e.g. in Fig. 3 panel above the bottom one. The geomagnetic storm was ongoing during the 7 September, but its main phase occurred only early on the 8 September. Despite such strong impulse preceded by the full active day, the ionospheric response in the topside sector at polar and auroral latitudes was not immediate as intensifications in Fig. 4 demonstrate. This Fig. 4 reports the same quantities of Fig. 3, but for the conditions already after the storm onset. First panel shows *Ne* data chop covering the investigated high latitude sectors. This Swarm track refers to the southern hemisphere, as crossed between 00:10 UT and 00:30 UT on 8 September 2017. The second panel shows IMFogram where one can identify the specific scales (e.g., at 100 km scale) including slightly increased levels of background activity compared

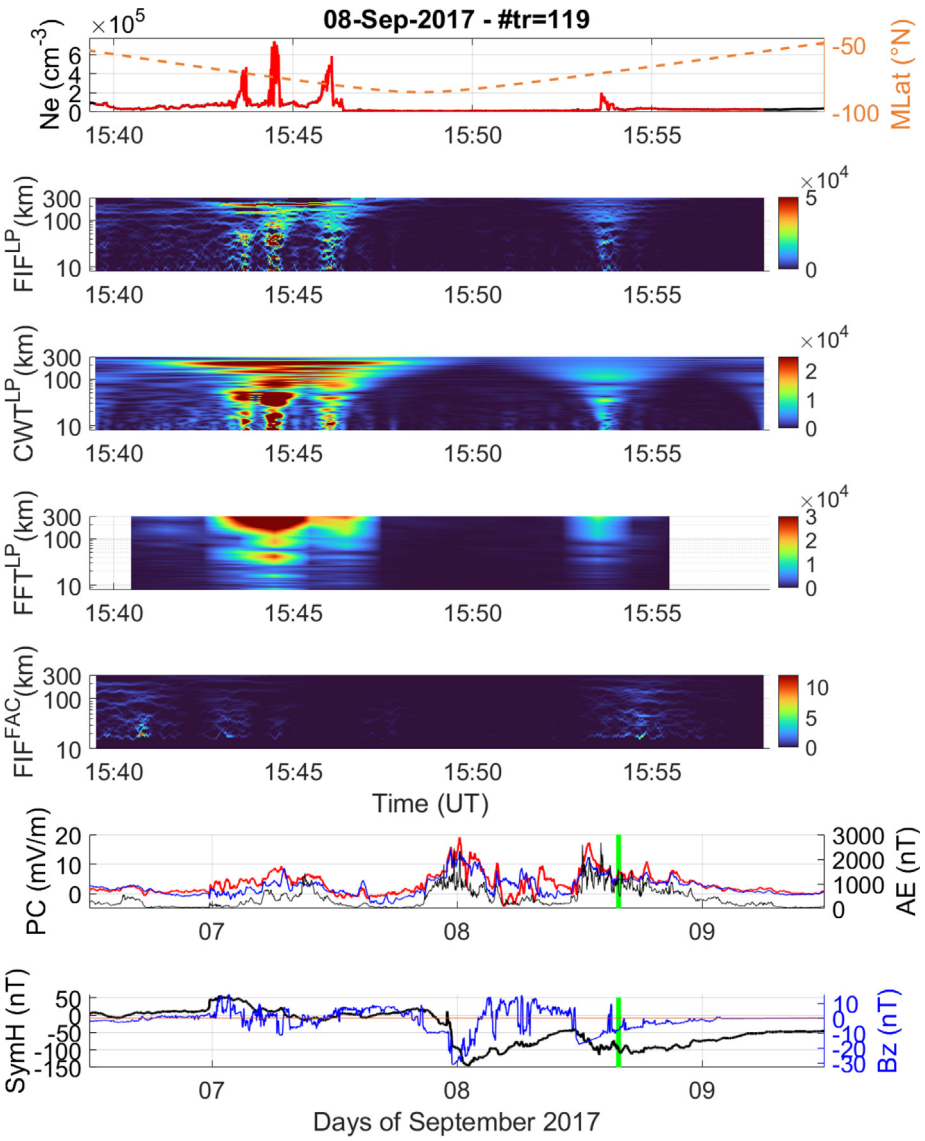

Fig. 5. Storm main phase and ionospheric plasma scale intensifications: Top panel shows the 2 Hz LP electron density measurements, following 3 middle panels demonstrate the intensities of scales constructed by FIF, CWT and FFT, respectively. Following IMFogram shows the intensities of the FAC. Last two panels show the high-latitude geomagnetic activity (The AE, the PC North and PC South indices are printed in black, blue, and red, resp.), SymH and the IMF Bz conditions, where the green lines indicate the time of the Swarm track.

to the quiescent conditions shown in respective panel of Fig. 3.

The following geomagnetic storm reached its maximum phase at around 14 UT on 8 September, which finally resulted in significantly stronger ionospheric effects as summarized by Figs. 5, 1, associated with slightly stronger AE activity, but possibly also the negative ionospheric storm compared to previous positive storm development.

The Fig. 5 reports the same quantities of Figs. 3,4, but for the conditions during the ongoing second storm. This Swarm track again refers to the southern hemisphere, as crossed between 15:39 UT and 15:58 UT on 8 September 2017. Its second panel shows IMFogram with many significantly increased levels of *Ne* scales activity compared to the first part of the storm shown in respective panel of Fig. 4. S4 enhancements visible at ground from SANAE and DMC (Concordia) station support the presence of small-scale irregularities (D'Angelo et al., 2021). In the paper they report about Swarm tracks in the field of view of Concordia.

The second storm recovery snapshot was provided in Fig. 1 with interval of 20:22 UT and 20:42 UT on 8 September 2017.

In the following, we use track-length normalised track-integrated IMFograms, allowing us to provide quasi-continuous analysis of the ionospheric *Ne* scales intensifications at the high latitudes during the whole month of September 2017 and focus on its most intense part of 5–11 September in Figs. 6, 7, respectively. From those we infer that intensifications of 8 September showed significantly different effects at high-latitudes of the both hemispheres which is best comparable looking at those track-

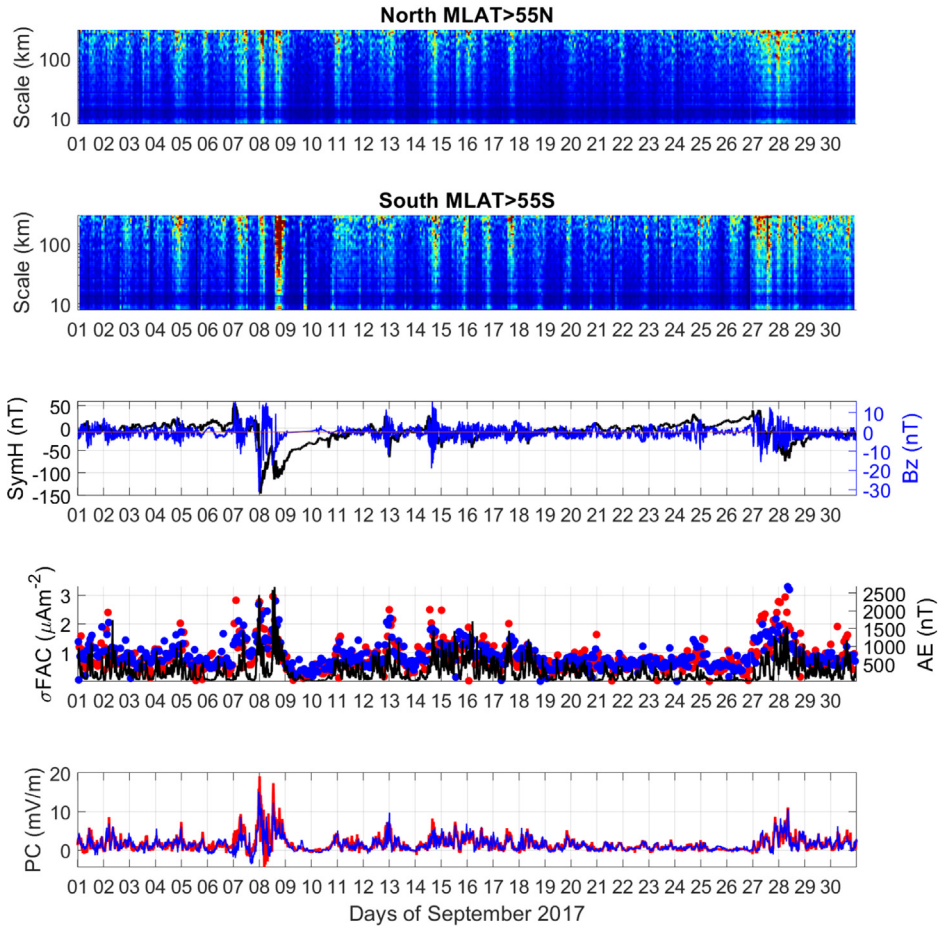

Fig. 6. Track-length normalised integrated Swarm A plasma density fluctuation intensifications (two upper panels) during September 2017. Middle panel with SymH index showing the storm conditions initiated by the interplanetary magnetic field North-South component (Bz, in blue), in following panel are overploted by the AE index the standard deviations of FAC over the selected tracks (in Northern and Southern high latitude, as blue and red circles, respectively). The bottom panel shows the polar cap activity indices (PC North and South in blue and red, respectively).

integrated representations of original IMFograms at two upper panels (each for respective hemisphere) in Figs. 6, 7. This hemispheric asymmetry might be related to strong density fluctuations observed above the Antarctic mainly around December solstice (Jin et al., 2020) associated with high levels of ionization and a strong variability of plasma dynamics (D'Angelo et al., 2021), with the other sources of hemispherical asymmetries reviewed in (Hatch et al., 2020). The recovery phase of the storm from 9 September did not render any significant intensifications. In the case studies shown (see Figs. 1–5) representing the storm development, we have focused on the Southern hemisphere, where the intensifications were more pronounced due to hemispherical asymmetries noted above along with the stronger southern polar magnetic activity, demonstrated by PCS compared to smaller PCN variation. That was valid during most of the September 2017 as bottom panel of Fig. 7 demonstrates, but most importantly, that is not supported by the σFAC also per respective track (see panel overplotting it with AE at Figs. 6, 7) not showing higher track-σFAC (in red) at period of most significant intensifications at Southern hemisphere of late September 8. The σFAC were plotted only when at least 50% of FAC data points from respective track were available to properly benchmark the intensity of those currents.

Mean values of the Solar Zenith Angle (SZA) calculated from these Swarm A selected measurements over Northern and Southern high latitudes ($|MLAT| > 55°$) were harmonically varying close to 82° but more fluctuating around 100°, respectively during early September 2017, but close to SZA 90° similarly at both hemispheres during equinoctial late September 2017. SZA daily variation was more pronounced in the Southern hemisphere mainly from the start of the month (due to reasons given above established in (Jin et al., 2020)) which may explain in part the higher level of Southern hemisphere intensifications, also relating them to the ratio of mid-latitude ionospheric measurements actually included into the auroral and polar cap (PC) data. The non-intensified tracks in Fig. 7 panel 2 representing Southern high-latitudes refer to the (artificially) shorter track representing lower SZA, e.g. on September 9 after 13 UT and on September 7 after 19 UT (SZA 80°). Analysis of this period with the knowledge of the GOES fluxes (shown for this period, e.g., in (Mosna et al., 2020)) also confirms that the occurrence of such exceptional solar flare forcing X-ray (EUV fluxes) does not have instantaneous

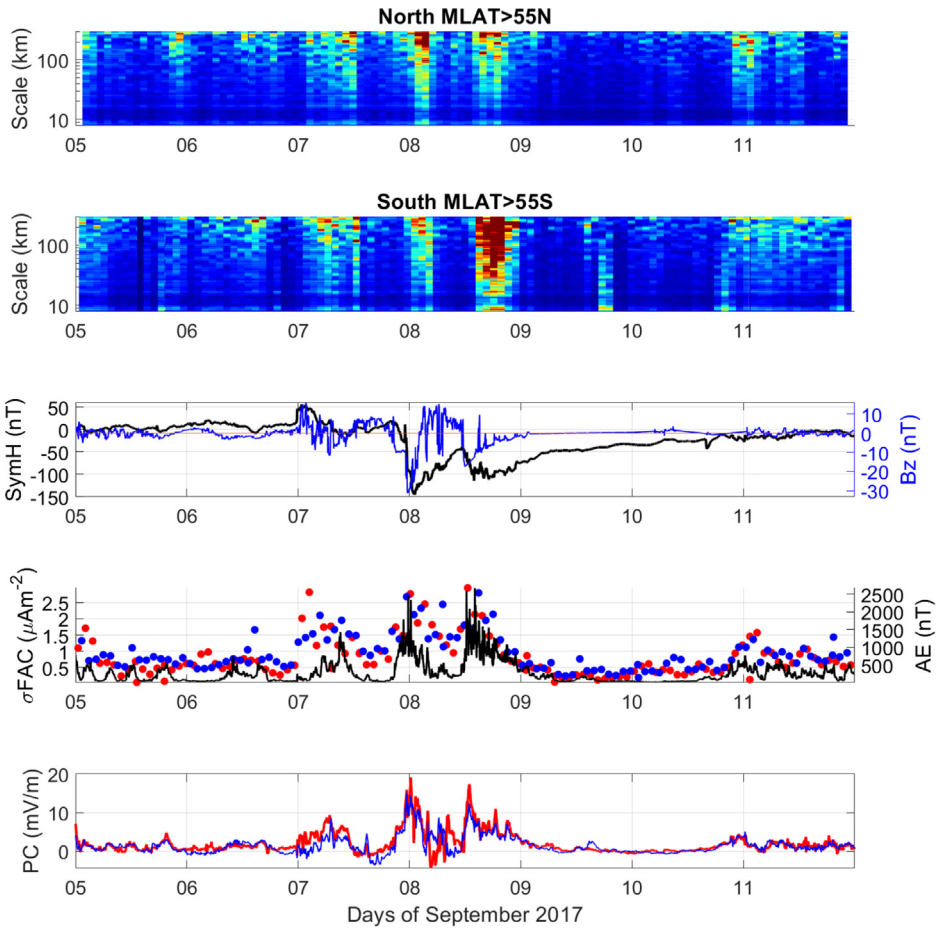

Fig. 7. Track-length normalised integrated Swarm A plasma density fluctuation intensification (two upper panels) focused on the September 2017 storm period. Middle panel with SymH index showing the storm conditions initiated by the interplanetary magnetic field North-South component (Bz, in blue), in following panel are overploted by the AE index the standard deviations of FAC over the selected tracks (in Northern and Southern high latitude, as blue and red circles, respectively). In the bottom panel are the polar cap activity indices (PC North and South in blue and red, respectively).

notable effect on the level of intensifications in the high-latitude ionosphere.

5. Conclusions

The intensifications of ionospheric plasma density fluctuation scales at topside high-latitude ionosphere are well highlighted by the novel concept, also showing significant delay in response to geomagnetic storm development.

The analysis of Swarm Ne suggested there is no (narrow-band) peculiar mode turning on, unlike it was possible to obtain in (Piersanti et al., 2017) or (Spogli et al., 2019) using other ionospheric parameters. That is associated with the complex coupling and resulting cascading processes involved in high-latitude ionospheric physics, not preferring specific resonance modes.

We evaluated the range of geophysical factors potentially influencing the intensifications. As the FAC connects the magnetosphere and ionosphere at high latitudes, it constraints various related physical parameters, e.g., ionospheric conductivity.

Except the stated delay, the AE and PC were found as a best proxy of the ionospheric activity of the investigated kind. The Swarm IPIR products grad Ne@100 km, grad Ne@50 km and grad Ne@20 km represent the trend of changes reasonably similarly as the FIF scales intensification at those selected scales (see Fig. 2), but the FIF provides the information about whole range of scales with significantly higher spatio-temporal resolution. The timeline of intensification in the Southern hemisphere (Figs. 6, 7) is more influenced by greater range of MLT and SZA during the Swarm passes comparing to the Northern hemisphere, but the main difference is still due to interhemispheric asymmetry, not only during storm conditions, but especially during low solar activity (Kotova et al., 2022).

The analysis uncovered the range of frequencies embedded in Swarm plasma density data being primarily enhanced under increased geospace forcing, specifically around 200, 100 and 30–50 km in spatial (North-South) scales (due to Swarm polar orbit). The cascading process of the ionospheric plasma then spread to smaller scale lengths, possibly through large scale changes in the ionosphere or local plasma processes of, e.g., kinetic nature,

deviating from Kolmogorov's 5/3 turbulence slope. There are range of cascading processes that can be involved (Guio and Pécseli, 2021; De Michelis et al., 2021), but at the current stage of the development of our technique, we are not able to identify the kind of cascading process.

The use of FIF is limiting the diffusion initiated by the jumps in the data, which is best shown comparing the IMFogram with classical spectrograms (which tries to compensate and smear the effect). As we have identified intensifications at specific scales amid the cascading, those can relate with the proxies which could act scale-wise due to physical processes.

The activity shown by *Ne* IMFograms relate to the wave processes seen in FAC with a delay which will be subject of the further research aiming to compare the lags of the intensification in the common scales between the plasma density measurements and the field-aligned current measurements between the leading and trailing satellite (Swarm A-C pair) in the high-latitude regions. The concept of evaluation of scale-wise lags from the data of Swarm A-C pair was already addressed in (Urbar et al., 2021). Having the information about lags between Swarm plasma density and FAC intensifications, their (scale-dependent) drivers can be more reliably identified.

This overall concept allows statistical characterization of different ionospheric storms and provision of climatology of scales by including longer datasets.

Declaration of Competing Interest

The authors declare that they have no known competing financial interests or personal relationships that could have appeared to influence the work reported in this paper.

Acknowledgments

Jaroslav Urbar gratefully acknowledges the postdoctoral research fellowship awarded by the PNRA (National Antarctic Research Program) (PNRA 14/00133 - PNRA 14/00110). Antonio Cicone is a member of the Italian "Gruppo Nazionale di Calcolo Scientifico" (GNCS) of the Istituto Nazionale di Alta Matematica "Francesco Severi" (INdAM) and affiliated with the Istituto di Astrofisica e Planetologia Spaziali, INAF, Rome, Italy. This work is part of the activities conducted in the frame of the Swarm Space Weather Variability of Ionospheric Plasma (Swarm VIP) project, that has been funded by the European Space Agency, contract 4000130562/20/I-DT with the title "Swarm+4D Ionosphere".

Appendix A. Swarm plasma density data products

We state here reasons for the selection of the specific LP plasma density data products as there are some differences between them. We selected the LP OPER, which is adopted throughout the paper due to various reasons, mainly noise filtering (see Fig. 8). Nevertheless, we have not checked whether there were any swaps between the specific low-/high-gain probes being used for the specific interval of September 2017 used for our analysis as The Extended LP dataset (v0101) and OPER (v0501) seems to be identical till 28th Feb 2017, after then it differ significantly. The flag indicators were tested for removing measurements during unreliable conditions, nevertheless also for this event they did not removed the spiky noise-like signal.

LP shows a good agreement with the FP, except having an offset during the measurements on the night-side (see Fig.8 in (Catapano et al., 2022)). That seems to be mainly related to the fact that the LP processing currently assumes

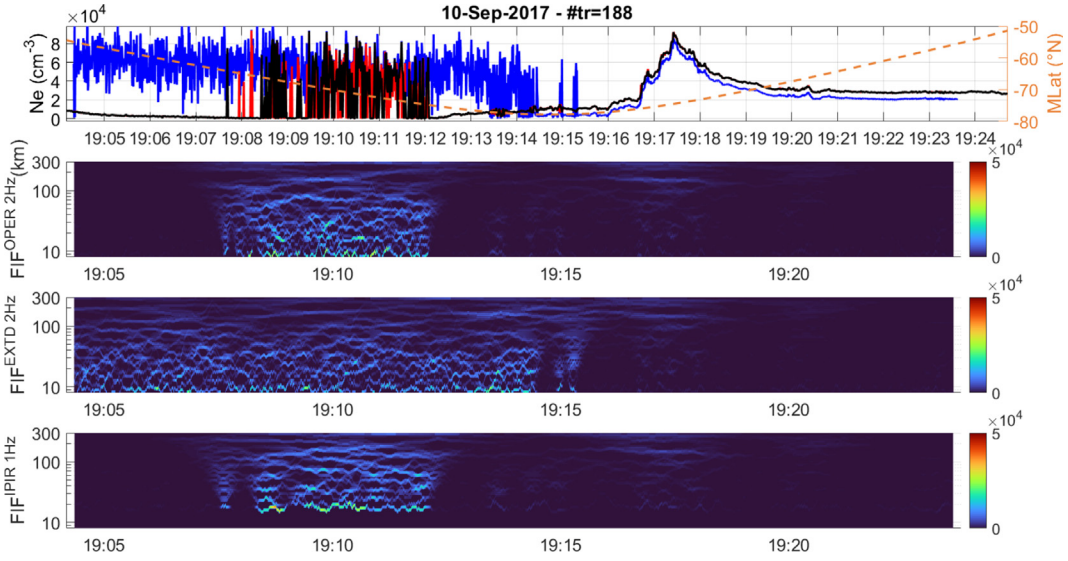

Fig. 8. Comparison of Swarm LP data products: Top panel shows the plasma density as provided by 2 Hz OPER (being used as LP data throughout the paper), 2 Hz EXTENDED, and 1 Hz IPIR, in red, blue, and black, respectively. The following panels demonstrate their respective scale intensities by IMFograms.

plasma being composed of singly ionised oxygen (Catapano et al., 2022). Additionally, as FP acts as planar LP detector, there is higher possibility of the sunlight contamination. These reasons were instrumental for use of LP measurements for statistical purposes, together with the significantly lower data availability and not intensified scales in the lowest spatial range observable only by FP.

References

Aa, E., Huang, W., Liu, S., Ridley, A., Zou, S., Shi, L., Chen, Y., Shen, H., Yuan, T., Li, J., Wang, T., 2018. Midlatitude plasma bubbles over china and adjacent areas during a magnetic storm on 8 september 2017. Space Weather 16 (3), 321–331. https://doi.org/10.1002/2017SW001776.

Alfonsi, L., Cesaroni, C., Spogli, L., Regi, M., Paul, A., Ray, S., Lepidi, S., Di Mauro, D., Haralambous, H., Oikonomou, C., Shreedevi, P.R., Sinha, A.K., 2021. Ionospheric disturbances over the indian sector during 8 september 2017 geomagnetic storm: Plasma structuring and propagation. Space Weather 19(3), e2020SW002607. https://doi.org/10.1029/2020SW002607.

Berdermann, J., Kriegel, M., Banys, D., Heymann, F., Hoque, M.M., Wilken, V., Borries, C., Heßelbarth, A., Jakowski, N., 2018. Ionospheric response to the x9.3 flare on 6 september 2017 and its implication for navigation services over europe. Space Weather 16 (10), 1604–1615. https://doi.org/10.1029/2018SW001933.

Buchert, S., Nilsson, T., 2017. Extended efi lp data fp release notes. Swarm Expert Support Laboratories (3). https://earth.esa.int/eogateway/documents/20142/37627/SW-RN-IRF-GS-005_Extended_LP_Data_Probes.pdf.

Catapano, F., Buchert, S., Qamili, E., Nilsson, T., Bouffard, J., Siemes, C., Coco, I., D'Amicis, R., Tøffner-Clausen, L., Trenchi, L., Holmdahl Olsen, P.E., Stromme, A., 2022. Swarm langmuir probes' data quality validation and future improvements. Geosci. Instrument. Methods Data Syst. 11 (1), 149–162. https://doi.org/10.5194/gi-11-149-2022.

Cicone, A., 2020. Iterative filtering as a direct method for the decomposition of nonstationary signals. Numer. Algor. 85 (3), 811–827. https://doi.org/10.1007/s11075-019-00838-z.

Cicone, A., Li, W., Zhou, H., 2022. New theoretical insights in the decomposition and time-frequency representation of nonstationary signals: the imfogram algorithm. IEEE Trans. Signal Process. https://doi.org/10.48550/arXiv.2205.15702, in review.

Cicone, A., Liu, J., Zhou, H., 2016. Adaptive local iterative filtering for signal decomposition and instantaneous frequency analysis. Appl. Comput. Harmon. Anal. 41 (2), 384–411. https://doi.org/10.1016/j.acha.2016.03.001.

Cicone, A., Pellegrino, E., 2022. Multivariate fast iterative filtering for the decomposition of nonstationary signals. IEEE Trans. Signal Process. 70, 1521–1531. https://doi.org/10.1109/TSP.2022.3157482, Conference Name: IEEE Transactions on Signal Processing.

Cicone, A., Zhou, H., 2021. Numerical analysis for iterative filtering with new efficient implementations based on FFT. Numer. Math. 147 (1), 1–28. https://doi.org/10.1007/s00211-020-01165-5.

D'Angelo, G., Piersanti, M., Pignalberi, A., Coco, I., De Michelis, P., Tozzi, R., Pezzopane, M., Alfonsi, L., Cilliers, P., Ubertini, P., 2021. Investigation of the physical processes involved in GNSS amplitude scintillations at high latitude: A case study. Remote Sens. 13(13), 2493. https://doi.org/10.3390/rs13132493. Number: 13 Publisher: Multidisciplinary Digital Publishing Institute.

Friis-Christensen, E., Lühr, H., Knudsen, D., Haagmans, R., 2008. Swarm – an earth observation mission investigating geospace. Adv. Space Res. 41 (1), 210–216. https://doi.org/10.1016/j.asr.2006.10.008.

Materassi, M., Piersanti, M., Consolini, G., Diego, P., D'Angelo, G., Bertello, I., Cicone, A., 2019. Stepping into the equatorward boundary of the auroral oval: preliminary results of multi scale statistical analysis. Ann. Geophys. 62(4), GM455–GM455. https://doi.org/10.4401/ag-7801. Number: 4.

De Michelis, P., Consolini, G., Pignalberi, A., Tozzi, R., Coco, I., Giannattasio, F., Pezzopane, M., Balasis, G., 2021. Looking for a proxy of the ionospheric turbulence with swarm data. Sci Rep. 11(1), 6183. https://doi.org/10.1038/s41598-021-84985-1. Number: 1 Publisher: Nature Publishing Group.

Ghobadi, H., Savas, C., Spogli, L., Dovis, F., Cicone, A., Cafaro, M., 2020. A comparative study of different phase detrending algorithms for scintillation monitoring. In: 2020 XXXIIIrd General Assembly and Scientific Symposium of the International Union of Radio Science, pp. 1–4. https://doi.org/10.23919/URSIGASS49373.2020.9232349. ISSN: 2642-4339.

Ghobadi, H., Spogli, L., Alfonsi, L., Cesaroni, C., Cicone, A., Linty, N., Romano, V., Cafaro, M., 2020b. Disentangling ionospheric refraction and diffraction effects in GNSS raw phase through fast iterative filtering technique. GPS Solut. 24 (3), 85. https://doi.org/10.1007/s10291-020-01001-1, URL: https://doi.org/10.1007/s10291-020-01001-1.

Guio, P., Pécseli, H.L., 2021. The impact of turbulence on the ionosphere and magnetosphere. In: Frontiers in Astronomy and Space Sciences, p. 7, URL: https://www.frontiersin.org/article/10.3389/fspas.2020.573746.

Hatch, S.M., Haaland, S., Laundal, K.M., Moretto, T., Yau, A.W., Bjoland, L., Reistad, J.P., Ohma, A., Oksavik, K., 2020. Seasonal and hemispheric asymmetries of f region polar cap plasma density: Swarm and CHAMP observations. J. Geophys. Res. Space Phys. 125 (11). https://doi.org/10.1029/2020JA028084 e2020JA028084.

Jimoh, O., Lei, J., Zhong, J., Owolabi, C., Luan, X., Dou, X., 2019. Topside ionospheric conditions during the 7–8 september 2017 geomagnetic storm. J. Geophys. Res. (Space Phys.) 124, 9381–9404. https://doi.org/10.1029/2019JA026590. ADS Bibcode: 2019JGRA.124.9381J.

Jin, Y., Kotova, D., Xiong, C., Brask, S., Clausen, L.B.N., Kervalishvili, G., Stolle, C., Miloch, W.J., 2022. Ionospheric plasma IRregularities - IPIR - data product based on data from the swarm satellites. J. Geophys. Res. Space Phys. n/a. https://doi.org/10.1029/2021JA030183 e2021JA030183.

Jin, Y., Xiong, C., Clausen, L., Spicher, A., Kotova, D., Brask, S., Kervalishvili, G., Stolle, C., Miloch, W., 2020. Ionospheric plasma irregularities based on in situ measurements from the swarm satellites. J. Geophys. Res. Space Phys. 125 (7). https://doi.org/10.1029/2020JA028103 e2020JA028103.

Kauristie, K., Morschhauser, A., Olsen, N., Finlay, C.C., McPherron, R. L., Gjerloev, J.W., Opgenoorth, H.J., 2017. On the usage of geomagnetic indices for data selection in internal field modelling. Space Sci. Rev. 206 (1), 61–90. https://doi.org/10.1007/s11214-016-0301-0.

Kervalishvili, G., Park, J., 2017. Swarm l2 fac-single product description. Swarm Expert Support Laboratories (5). https://earth.esa.int/eogateway/documents/20142/37627/swarm-level-2-fac-single-product-description.pdf.

Knudsen, D.J., Burchill, J.K., Buchert, S.C., Eriksson, A.I., Gill, R., Wahlund, J.-E., Åhlen, L., Smith, M., Moffat, B., 2017. Thermal ion imagers and langmuir probes in the swarm electric field instruments. J. Geophys. Res. Space Phys. 122 (2), 2655–2673. https://doi.org/10.1002/2016JA022571.

Kotova, D., Jin, Y., Miloch, W., 2022. Interhemispheric variability of the electron density and derived parameters by the Swarm satellites during different solar activity. J. Space Weather Space Clim. https://doi.org/10.1051/swsc/2022007.

Li, G., Ning, B., Wang, C., Abdu, M.A., Otsuka, Y., Yamamoto, M., Wu, J., Chen, J., 2018. Storm-enhanced development of postsunset equatorial plasma bubbles around the meridian 120e/60w on 7–8 september 2017. J. Geophys. Res. Space Phys. 123 (9), 7985–7998. https://doi.org/10.1029/2018JA025871.

Linty, N., Minetto, A., Dovis, F., Spogli, L., 2018. Effects of phase scintillation on the GNSS positioning error during the september 2017

storm at svalbard. Space Weather 16 (9), 1317–1329. https://doi.org/10.1029/2018SW001940.

Moen, J., Carlson, H.C., Rinne, Y., Skjæveland, A., 2012. Multi-scale features of solar terrestrial coupling in the cusp ionosphere. J. Atmos. Solar Terr. Phys. 87–88, 11–19. https://doi.org/10.1016/j.jastp.2011.07.002.

Mosna, Z., Kouba, D., Knizova, P.K., Buresova, D., Chum, J., Sindelarova, T., Urbar, J., Boska, J., Saxonbergova–Jankovicova, D., 2020. Ionospheric storm of september 2017 observed at ionospheric station pruhonice, the czech republic. Adv. Space Res. 65 (1), 115–128. https://doi.org/10.1016/j.asr.2019.09.024.

Perrone, L., Franceschi, G.D., 1998. Solar, ionospheric and geomagnetic indices. Ann. Geophys. 41 (5), 5–6. https://doi.org/10.4401/ag-3824.

Piersanti, M., Cesaroni, C., Spogli, L., Alberti, T., 2017. Does TEC react to a sudden impulse as a whole? the 2015 saint patrick's day storm event. Adv. Space Res. 60 (8), 1807–1816. https://doi.org/10.1016/j.asr.2017.01.021.

Piersanti, M., Materassi, M., Cicone, A., Spogli, L., Zhou, H., Ezquer, R. G., 2018. Adaptive local iterative filtering: A promising technique for the analysis of nonstationary signals. J. Geophys. Res. Space Phys. 123 (1), 1031–1046. https://doi.org/10.1002/2017JA024153.

Ritter, P., Lühr, H., Rauberg, J., 2013. Determining field-aligned currents with the swarm constellation mission. Earth Planet Sp. 65 (11), 9. https://doi.org/10.5047/eps.2013.09.006.

Shinbori, A., Otsuka, Y., Sori, T., Tsugawa, T., Nishioka, M., 2020. Temporal and spatial variations of total electron content enhancements during a geomagnetic storm on 27 and 28 september 2017. J. Geophys. Res. Space Phys. 125(7), e2019JA026873. https://doi.org/10.1029/2019JA026873.

Smith, C., L'Heureux, J., Ness, N., Acuña, M., Burlaga, L., Scheifele, J., 1998. The ACE magnetic fields experiment. Space Sci. Rev. 86 (1), 613–632. https://doi.org/10.1023/A:1005092216668.

Spogli, L., Piersanti, M., Cesaroni, C., Materassi, M., Cicone, A., Alfonsi, L., Romano, V., Ezquer, R.G., 2019. Role of the external drivers in the occurrence of low-latitude ionospheric scintillation revealed by multi-scale analysis. J. Space Weather Space Clim. 9, A35. https://doi.org/10.1051/swsc/2019032.

Stallone, A., Cicone, A., Materassi, M., 2020. New insights and best practices for the successful use of empirical mode decomposition, iterative filtering and derived algorithms. Sci. Rep. 10(1), 15161. https://doi.org/10.1038/s41598-020-72193-2. Number: 1 Publisher: Nature Publishing Group.

Tassev, Y., Velinov, P., Mateev, L., Tomova, D., 2018. Analysis of extreme solar activity in early september 2017: G4 - severe geomagnetic storm (07–0809) and GLE72 (1009) in solar minimum. Comptes Rendus de l'Academie Bulgare des Sciences 70(10), 1437–1444. Place: Bulgaria INIS Reference Number: 49007004.

Troshichev, O., Janzhura, A., Stauning, P., 2006. Unified PCN and PCS indices: Method of calculation, physical sense, and dependence on the IMF azimuthal and northward components. J. Geophys. Res. Space Phys. 111. https://doi.org/10.1029/2005JA011402.

Urbar, J., Cicone, A., Spogli, L., Cesaroni, C., Alfonsi, L., 2021. Intrinsic mode cross correlation: A novel technique to identify scale-dependent lags between two signals and its application to ionospheric science. In: IEEE Geosci. Remote Sens. Lett., 19. Publisher Name: IEEE Geoscience and Remote Sensing Letters, pp. 1–3. https://doi.org/10.1109/LGRS.2021.3122108.

Wu, C.-C., Liou, K., Lepping, R.P., Hutting, L., 2019. The 04–10 september 2017 sun–earth connection events: Solar flares, coronal mass ejections/magnetic clouds, and geomagnetic storms. Sol. Phys. 294 (8), 110. https://doi.org/10.1007/s11207-019-1446-2.